

X-RAY PLASMA EJECTION ASSOCIATED WITH AN IMPULSIVE FLARE ON 1992 OCTOBER 5: PHYSICAL CONDITIONS OF X-RAY PLASMA EJECTION

MASAMITSU OHYAMA¹

Institute of Space and Astronautical Science, Sagami-hara, Kanagawa 229-8510, Japan; ohyama@solar.mtk.nao.ac.jp

AND

KAZUNARI SHIBATA

National Astronomical Observatory, Mitaka, Tokyo 181-8588, Japan

Received 1997 February 25; accepted 1998 January 7

ABSTRACT

The 1992 October 5 flare was associated with an X-ray plasma ejection. Although the ejected plasma looks like a blob (or plasmoid) in short-exposure images, in long-exposure images it appears to be penetrated by or connected to the top of a large-scale loop. The ejecta had started to rise with a speed of $\sim 250 \text{ km s}^{-1}$ before the main peak of the hard X-ray emission and was accelerated during the impulsive phase (to $\sim 500 \text{ km s}^{-1}$). We derived the physical parameters of the ejected plasma and obtained the following results: (1) The temperature of the ejected plasma was $10.6 \pm 3.6 \text{ MK}$. (2) Its density was $(8\text{--}16) \times 10^9 \text{ cm}^{-3}$ and was an order of magnitude larger than that of the typical active-region corona. (3) The mass of the ejected plasma was $(2\text{--}4) \times 10^{13} \text{ g}$. (4) The kinetic energy of the ejecta was smaller than the thermal energy content of the flare loop. The overall features and evolution of the hot plasma ejection and flare are in rough agreement with those expected from the reconnection model, and the reconnection rate ($M_A = V_{\text{in}}/V_A$) is estimated to be ~ 0.02 , where V_{in} is the speed of the inflow into the reconnection region, and V_A is the Alfvén speed. Result 4, however, is not consistent with the assumption in some reconnection models that an ejected plasma stretches the overlying magnetic fields to form a current sheet and hence leads to magnetic reconnection. Instead, our results suggest that both X-ray plasma ejection and reconnection are a consequence of a common dynamical process such as the global MHD instability.

Subject headings: Sun: activity — Sun: corona — Sun: flares — Sun: X-rays, gamma rays

1. INTRODUCTION

Researchers examining data from the soft X-ray telescope (Tsuneta et al. 1991) aboard *Yohkoh* (Ogawara et al. 1991) have discovered that long-duration event (LDE) flares, defined as flares lasting for more than 1 hr in the *GOES* total intensity plot (e.g., Kosugi & Shibata 1997), show cusp-shaped loop and arcade structures and that the outer cusp-shaped loops have systematically higher temperatures (Tsuneta et al. 1992; Tsuneta 1996; Švestka et al. 1995; Forbes & Acton 1996). X-ray plasma ejections have often been found to be associated with these LDE flares (e.g., Hudson 1994; Švestka et al. 1995). These observations are consistent with the prediction by magnetic reconnection models in which reconnection is assumed to take place in the vertical current sheet above flare loops (see, e.g., Carmichael 1964; Sturrock 1966; Hirayama 1974; Kopp & Pneuman 1976; Forbes & Priest 1982; Ugai 1989; Moore & Roumeliotis 1992; Magara et al. 1996; Yokoyama & Shibata 1997).

In contrast, no cusp-shaped structures are seen in soft X-ray images of impulsive flares, defined as flares lasting for less than 1 hr in the *GOES* plot in this paper, and thus it was thought that impulsive flares might not be explained by the reconnection model. Masuda et al. (1994, 1995), however, have discovered compact impulsive hard X-ray (HXR) sources *above* the soft X-ray flare loop in some impulsive limb flares. Moreover, in the same flares, Shibata et al. (1995) found X-ray plasma ejections moving upward at about $50\text{--}400 \text{ km s}^{-1}$ above soft X-ray flare loops and the

above-the-loop-top HXR sources. Similar X-ray plasma ejections have been found in other impulsive, compact flares (see, e.g., Tsuneta 1993, 1997; Nitta 1996; Ohyama & Shibata 1997; Ohyama et al. 1997). These discoveries suggest that impulsive flares occur through a magnetic reconnection process similar to that proposed for LDE flares (Shibata et al. 1995; Shibata 1996; Tsuneta et al. 1997).

It has often been suggested (see, e.g., Sturrock 1992) that an ejected plasma (prominence eruption) stretches the overlying magnetic fields to form a current sheet, leading to reconnection. This suggestion predicts that the kinetic energy of the ejected material would be larger than the magnetic energy, which is the energy released in flares.

In order to study the mechanism in impulsive flares and to test the hypothesis that an ejected plasma stretches the overlying magnetic field to form a current sheet, it is important to investigate the detailed structure and physical conditions of the ejecta associated with impulsive flares. In this study, we analyze the detailed physical conditions of the plasma ejection associated with the 1992 October 5 flare. The observing methods are summarized in § 2, and the analysis methods and results are described in detail in § 3. Finally, discussions of the morphology and physical conditions of the ejected material are given in § 4. This event was first reported by Akita (1994), and a preliminary report of the analysis was given by Ohyama & Shibata (1996).

2. OBSERVATIONS

An eruptive flare occurred behind the west limb on 1992 October 5. This flare was observed with the soft X-ray telescope (SXT) and the hard X-ray telescope (HXT) (Kosugi et

¹ Current address: National Astronomical Observatory, Mitaka, Tokyo 181-8588, Japan.

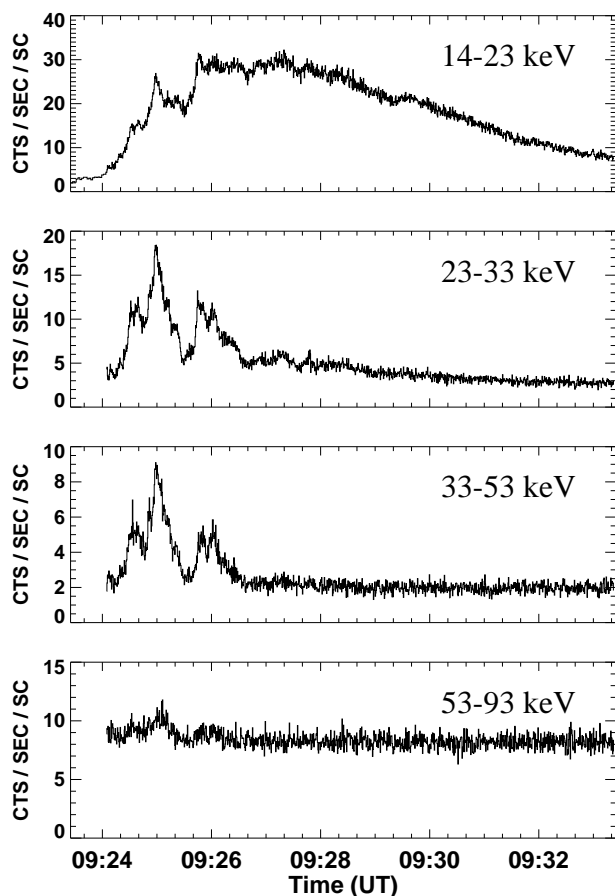


FIG. 1.—Hard X-ray time profiles of the flare on 1992 October 5. The intensities are measured in the four HXT energy bands in units of counts per second per subcollimator.

al. 1991) aboard *Yohkoh*. In this study, we will use the partial frame images that consist of 64×64 full-resolution ($2''.5$) pixels using the $0.1 \mu\text{m}$ (thin) and $12 \mu\text{m}$ (thick) aluminum and beryllium filters and of 64×64 half-resolution ($5''$) pixels using the thin aluminum filter.

3. ANALYSIS AND RESULTS

The eruptive flare that we study in this paper was classified as an M2.0 class flare² which took place behind the west limb (probably in NOAA 7293). A bright H α surge (or spray) occurred near the flare region between 09:15 UT and 09:25 UT, according to the Solar-Geophysical Data (1993, 584, Part II).

3.1. Morphological Evolution

Yohkoh observed this flare since 09:24:05 UT. Figure 1 shows the time profiles of the HXR intensity of the flare detected with four channels of HXT. It is seen that the hard X-ray emission was impulsive and that its lifetime was about 8 minutes. The evolution of the soft X-ray structure of this flare is shown in Figure 2. The thick curves indicate

² It should be noted that according to Solar-Geophysical Data (1993, 584, Part II), another flare whose H α importance was SF occurred in NOAA Active Region 7305 at N12°, E41° simultaneously (from 09:25 UT to 09:30 UT). Although the level of the total X-ray emissions of two flares in *GOES* data was M2.0, in this paper we classified the analyzed eruptive flare as M2.0 in X-rays because in NOAA AR 7305, some flares whose H α importance were SF occurred, and their X-ray class were below C2.0 in *GOES* X-ray.

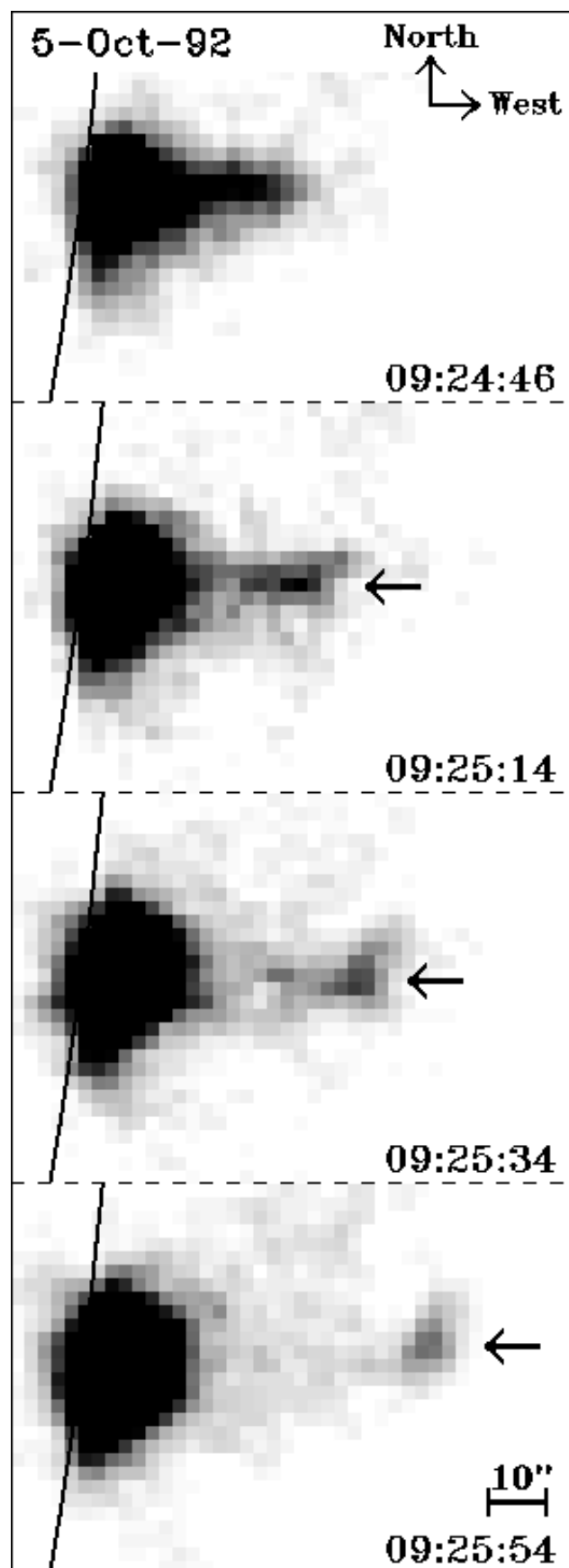


FIG. 2.—Sequence of SXT images of the flare on 1992 October 5. These images were taken with the thin aluminum filter and a 2.9 ms exposure. The ejected plasma is indicated by the arrows. The curves indicate the solar limb; $1''$ is ~ 726 km.

the western solar limb. A hot plasma, which is indicated by arrows, can be seen being ejected in a bloblike form (plasmoid). We cannot determine the initial position of the plasmoid because it was apparently hidden by the flare loop in the early stage, and its soft X-ray intensity was much weaker than the X-ray intensity of the flare loop(s). The apparent height of the plasmoid is shown in Figure 3 as a function of time. The plasmoid was ejected at an apparent velocity of $\sim 250 \text{ km s}^{-1}$, before the main peak of the hard X-ray emission, and was accelerated to $\sim 500 \text{ km s}^{-1}$ during the impulsive phase.

Figure 4 (Plate 23) shows half-resolution ($5''$) soft X-ray images taken with longer exposure times. These images show that the X-ray ejecta consisted of not only the plasmoid (P in Fig. 4) but also of an expanding loop (L). The expanding loop seemed to penetrate or be connected to the plasmoid. In two images, the plasmoid was seen to be at the top of the loop, and the loop expanded with the rise of the plasmoid, although there is a possibility that the two structures were separated along the direction of the line of sight. The intensity of the expanding loop was an order of magnitude weaker than that of the plasmoid (Fig. 5). Figure 4c shows another structure, an ellipsoidal loop around the plasmoid. A schematic picture of the image at 09:26:08 UT (Fig. 4c) is shown in Figure 4d.

3.2. Physical Conditions of the X-Ray Plasma Ejecta

We shall derive the physical parameters of the ejected material in this section. The ejected material consisted of not only the blob (plasmoid) but also the loop structure (see Fig. 4), and thus we should estimate the physical parameters

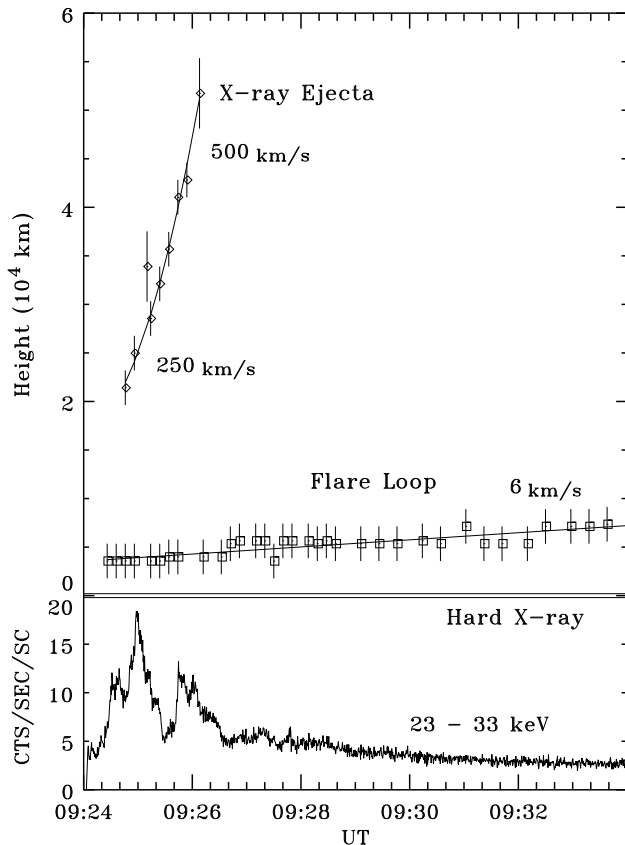


FIG. 3.—Apparent heights of the plasmoid and flare loop for the 1992 October 5 flare. Counting rates are from the 23–33 keV channel of HXT. Projected velocities are indicated.

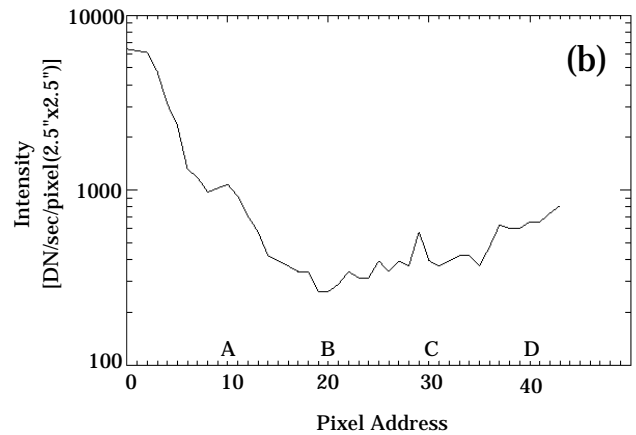
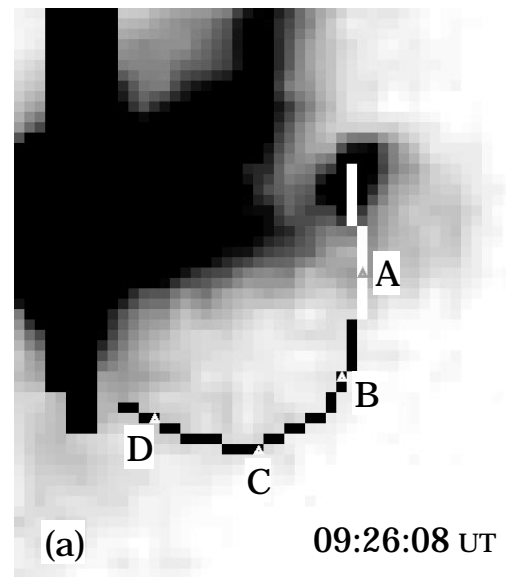


FIG. 5.—(a) Half-resolution image at 09:26:08 UT. (b) Intensity profile along the curve in (a); A, B, C, and D correspond to the positions given in (a).

of both. Since the plasmoid was observed with multiple filters (thin and thick aluminum and beryllium filters), we derive its physical parameters using the filter ratio method (Vaiana, Krieger, & Timothy 1973; Gerassimenko & Nolte 1978; Hara et al. 1992). We assume a filling factor of unity throughout this paper. Since the expanding loop was taken only with one filter (thin aluminum filter), we cannot use the filter ratio method in this case. Thus, at first the emission measure of the expanding loop is calculated by assuming that its temperature is equal to the derived temperature of the plasmoid. The other physical parameters of the expanding loop, such as density, pressure, mass, etc., are calculated from the assumed temperature and the derived emission measure on the assumption of the filling factor of unity.

3.2.1. The Plasmoid

We derive the temperature and emission measure of the plasmoid and flare loop from the X-ray images assuming isothermality and then calculate the other physical parameters assuming a line-of-sight length of 10^4 km . Since the intensity of the plasmoid was weak, we take 3×3 pixel sums of the intensity in order to improve photon statistics.

Figure 6 (Plate 24) shows the soft X-ray intensity, temperature, emission measure, and pressure maps of the flare obtained from the combination of the thick aluminum and beryllium filters. The level of the scattered light within the ejecta from the surrounding regions is estimated to be less than 20%.³ The temperature is higher in the outer region than in the flare loop (high emission measure or high pressure region), which is consistent with the temperature distribution in other flares (e.g., Tsuneta et al. 1992; Tsuneta 1996; Masuda 1994). The temperature of the plasmoid was about 10 MK; its emission measure and pressure were much lower than those of the flare loop. The X-ray intensity and emission measure of the inner region of the plasmoid were larger than those of its outer region. The distribution of the pressure in the plasmoid, however, is found to be nearly flat.

Figure 7 shows the intensity, temperature, emission measure, and pressure distributions along the lines defined in Figure 6. The error bars indicate the 1 σ level due to the photon noise. We define the boundary of the plasmoid and flare loop as the place at which intensities are equal to $1/e$ ($\approx 37\%$; *solid line*, Fig. 7) of the maximum intensity in the plasmoid and $1/e^4$ ($\approx 2\%$; *dashed line*) of the maximum intensity in the flare loop, respectively.⁴ The physical parameters of the plasmoid and flare loop at 09:25:00 and 09:25:18 (plasmoid only) UT assuming a line-of-sight length of 10^4 km are summarized in Table 1. The temperature of the plasmoid was $\sim 10.6 \pm 3.6$ MK. Its electron density was $\sim 8 \times 10^9$ to 1.6×10^{10} cm^{-3} and was an order of magnitude larger than the typical density of the active-region corona, 10^9 cm^{-3} . The mass and thermal energy content of the plasmoid were $\sim (2.3 \pm 0.2) \times 10^{13}$ g and $\sim (5.4 \pm 0.5) \times 10^{28}$ ergs at 09:25:00 UT and decreased slightly to $\sim (1.9 \pm 0.2) \times 10^{13}$ g and $\sim (4.3 \pm 0.6) \times 10^{28}$ ergs, respectively, at 09:25:18 UT. Its kinetic energy was estimated to be $\sim 8 \times 10^{27}$ to 2×10^{28} ergs using its velocity of 300–400 km s^{-1} and was smaller than its thermal energy content, which in turn was an order of magnitude smaller than the thermal energy content of the flare loop.

In the above analysis, the line-of-sight length of the plasmoid is assumed to be constant (10^4 km), since its three-

³ The level of the scattered light within the center of the plasmoid from the surrounding regions is estimated to be less than 4%.

⁴ If the intensity of the place between the ejecta and flare loop is stronger than $1/e$ of the maximum value of the ejecta (the boundary of the ejecta), the boundary between them is assumed to be the intensity saddle point between them.

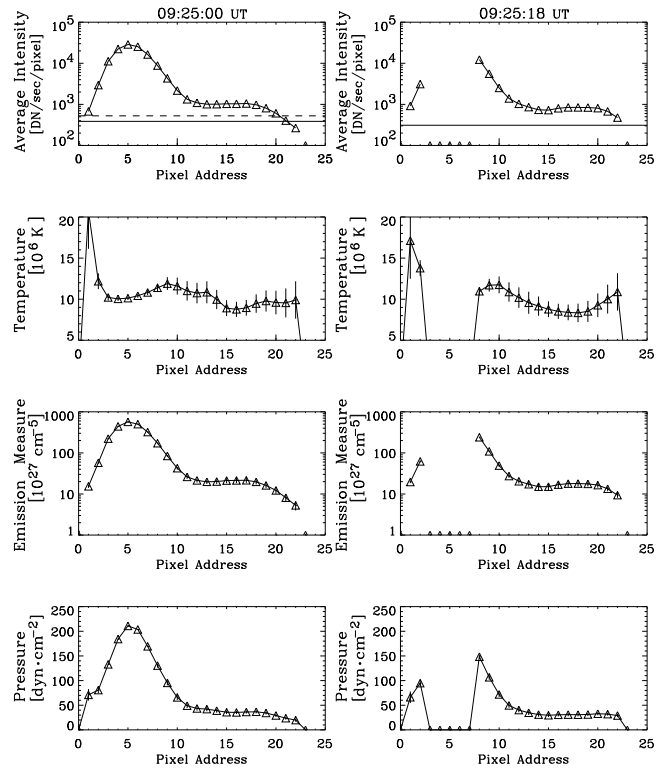


FIG. 7.—Intensity, temperature, emission measure, and pressure distributions along the lines in Fig. 6. The error bars indicate the 1 σ level due to the photon noise. The solid (dashed) line indicates the intensity $\sim 1/e$ ($1/e^4$) of the maximum value of the plasmoid (flare loop). The region of the plasmoid is between pixel address 14 and 21 at 09:25:00 UT and pixel address 15 and 22 at 09:25:18 UT.

dimensional structure is unknown. However, if the plasmoid is a structure such as a spheroid, its line-of-sight length would not be constant, and its density⁵ and pressure distribution will be different from the result of the above analysis. Thus, we shall calculate the physical parameters of the plasmoid, assuming that it is spheroidal. The value of the line-of-sight length corresponding to each pixel is given in the Appendix. Figure 8 shows the density and pressure

⁵ The density, n , is calculated by $n = (EM/l)^{1/2}$, where EM and l are the emission measure and line-of-sight length, respectively.

TABLE 1
PHYSICAL PARAMETERS OF THE PLASMOID (AT 09:25:00 AND 09:25:18 UT)
AND FLARE LOOP (AT 09:25:00 UT)

PHYSICAL PARAMETER	FLARE LOOP (09:25:00 UT)	PLASMOID	
		(09:25:00 UT)	(09:25:18 UT)
Temperature (10^6 K)	8.1–17.7	10.6 ± 3.6	9.8 ± 3.2
Emission measure (10^{28} cm^{-5})	10–580	6.3–25	7.3–20
Electron density (10^9 cm^{-3})	10–77	8–16	8.5–14
Gas pressure (dyn cm^{-2})	30–220	21–47	20–39
Mass (10^{13} g)	16.7 ± 0.5	2.3 ± 0.2	1.9 ± 0.2
Thermal energy content (10^{28} ergs)	47 ± 2.5	5.4 ± 0.5	4.3 ± 0.6
Kinetic energy ^a (10^{28} ergs)	—	1–2	0.8–1.6

^a Kinetic energy was calculated using the derived mass and a velocity of 300–400 km s^{-1} .

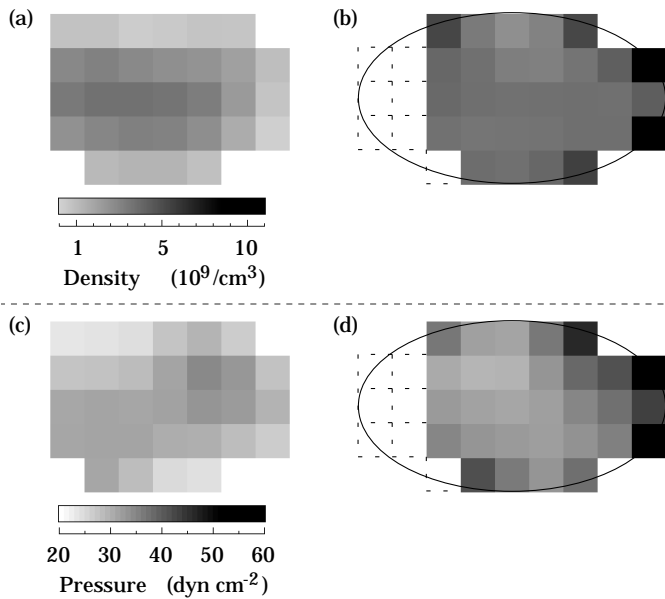


FIG. 8.—Density and pressure maps of the plasmoid, which is the region within the box in the X-ray image at 09:25:18 UT in Fig. 6. (a) Density map in the case of the assumption that the line-of-sight length is constant (10^4 km). (b) Density map in the case of the assumption that the plasmoid is spheroidal and that its line-of-sight length is not constant. (c) Pressure map in the case of the constant line-of-sight length. (d) Pressure map in the case of the nonconstant line-of-sight length.

maps of the plasmoid in the two cases. The density of its outer region is slightly smaller than that of its inner region when the line-of-sight length is constant, whereas in the case of the spheroid its density distribution is nearly flat. The pressure in the latter case is larger than that in the former case.

The physical parameters of the plasmoid in both cases are summarized in Table 2: the constant line-of-sight length in column (2) and the nonconstant line-of-sight length in columns (3) and (4). In the case of the assumption that the plasmoid is spheroidal, there is a possibility that part of the plasmoid, which is indicated by dashed boxes in Figure 8b, is not identified because part of the plasmoid was hidden by the flare loop, whose intensity was much stronger. Therefore, we also calculate the physical parameters of the plasmoid including the dashed boxes assuming the symmetry with respect to the minor axis (col. [4]). Though the density and gas pressure are larger in the case of the nonconstant line-of-sight length (spheroid) than in the case of constant line-of-sight length, the mass and thermal energy content

are less in the former case than in the latter case because the volume of the plasmoid is smaller in the former case.

3.2.2. The Expanding Loop

We shall estimate the physical parameters of the expanding loop assuming that its temperature was equal to the derived temperature of the plasmoid (7–14 MK), since it was observed only with one filter. (A similar method was used by Shibata et al. 1994 to estimate the mass of an X-ray jet.) Tables 3 and 4 summarize the physical parameters of the plasmoid and expanding loop derived from the half-resolution image at 09:26:08 UT assuming that the line-of-sight length is 10^4 km. Comparing the physical parameters of the plasmoid in Tables 1 and 3, we find that the physical parameters derived from the single filter image (Table 3) were consistent with those derived using the filter ratio method (Table 1), considering the effect of time evolution. It is found from Tables 3 and 4 that the density of the loop was smaller than that of the plasmoid. The mass, kinetic energy, and thermal energy content of the expanding loop were, however, factors of 2 or 3 larger than those of the plasmoid.

Although 10^4 km is used as the line-of-sight length of the plasmoid and expanding loop in above analysis, the width of the expanding loop seemed to be narrower than that of the plasmoid (Fig. 4c) and to be about 8×10^3 km. Thus, we shall examine the expanding loop in the case of its line-of-sight length being 8×10^3 km. The physical parameters of the expanding loop in such a case are summarized in Table 5, which shows that the density is slightly increased, while the mass, kinetic energy, and thermal energy content are slightly decreased. However, the mass and kinetic energy of the expanding loop were still larger than those of the plasmoid.

The thin aluminum filter, through which the half-resolution images were taken, is sensitive at temperatures lower than the ranges of sensitivity of the thick aluminum and beryllium filters. Therefore, we shall examine the physical parameters of the plasmoid and loop for two cases of their temperatures, 2 and 4 MK (Tables 3, 4, and 5). In the case of 4 MK, the estimated physical parameters are nearly equal to those for 7 MK. On the other hand, in the case of 2 MK, their density, mass, and kinetic energy are factors of 2 or 3 larger than those for 14 MK. It is found that the mass of the expanding loop was larger than that of the plasmoid for all cases of temperatures. Hence, even if an ejected plasma (a plasmoid) looks like a blob in short-exposure images, we should remember that the ejected plasma has a three-dimensional structure including not only the plasmoid but also the expanding loop. The kinetic energy of the

TABLE 2
PHYSICAL PARAMETERS OF THE PLASMOID AT 09:25:18 UT

PHYSICAL PARAMETER (1)	LINE-OF-SIGHT LENGTH		
	Constant (2)	NONCONSTANT (SPHEROID)	
		Observations (3)	Correction (4)
Electron Density (10^9 cm^{-3})	8.5–14	11–22	11–22
Gas Pressure (10^9 cm^{-3})	20–39	26–65	26–65
Mass (10^{13} g).....	1.9 ± 0.2	1.5 ± 0.1	1.8 ± 0.2
Thermal energy content (10^{28} ergs).....	4.3 ± 0.6	3.4 ± 0.4	4.1 ± 0.5

TABLE 3
PHYSICAL PARAMETERS OF THE PLASMOID DERIVED FROM THE
HALF-RESOLUTION IMAGE (09:26:08 UT)

Physical Parameter	2 MK	4 MK	7 MK	14 MK
Emission measure (10^{28} cm^{-5}).....	24–64	3.4–9	3.1–8.3	4.2–11
Electron density (10^9 cm^{-3}).....	15–25	5.8–9.5	5.6–9	6.5–10
Gas pressure (dyn cm^{-2}).....	8–14	6–10	10–18	25–40
Mass (10^{13} g).....	2.8	1.1	1	1.2
Thermal energy content (10^{28} ergs).....	1.4	1	1.8	4.1
Kinetic energy ^a (10^{28} ergs).....	3.5	1.4	1.3	1.5

NOTE.—Here it is assumed that the line-of-sight length of the plasmoid is 10^4 km .
^a Kinetic energy was calculated using the derived mass and velocity of 500 km s^{-1} .

X-ray ejecta including the expanding loop was still an order of magnitude smaller than the thermal energy content of the flare loop.

3.3. Time Evolution of the Flare Loop

The maps of soft X-ray intensity, temperature, emission measure, and pressure are shown in Figure 9 to illustrate

the time evolution of the flare loop. Consecutive images were summed so as to obtain better statistics and to show these quantities in the region in which the intensity was larger than $1/e^4$ ($\approx 2\%$) of the maximum intensity in the flare loop. The apparent height of the flare loop increased at a velocity of $\sim 6 \text{ km s}^{-1}$ (Figs. 3 and 9). The temperature appears to be higher in the outer region than in the flare

TABLE 4
PHYSICAL PARAMETERS OF THE EXPANDING LOOP DERIVED FROM THE
HALF-RESOLUTION IMAGE (09:26:08 UT)

Physical Parameter	2 MK	4 MK	7 MK	14 MK
Emission measure (10^{27} cm^{-5}).....	10–71	1.5–10	1.3–9	1.8–12
Electron density (10^9 cm^{-3}).....	3.2–8.4	1.2–3.2	1.2–3	1.3–3.5
Gas pressure (dyn cm^{-2}).....	1–5	1–4	2–6	5–14
Mass (10^{13} g).....	7.7	2.9	2.8	3.2
Thermal energy content (10^{28} ergs).....	3.8	2.9	4.8	11
Kinetic energy ^a (10^{28} ergs).....	9.7	3.6	3.5	4

NOTE.—Here it is assumed that the line-of-sight length of the expanding loop is 10^4 km .
^a Kinetic energy was calculated using the derived mass and velocity of 500 km s^{-1} .

TABLE 5
PHYSICAL PARAMETERS OF THE EXPANDING LOOP DERIVED FROM THE
HALF-RESOLUTION IMAGE (09:26:08 UT)

Physical Parameter	2 MK	4 MK	7 MK	14 MK
Emission measure (10^{27} cm^{-5}).....	10–71	1.5–10	1.3–9	1.8–12
Electron density (10^9 cm^{-3}).....	3.6–9.4	1.3–3.5	1.3–3.4	1.5–4
Gas pressure (dyn cm^{-2}).....	2–5	1–4	2–7	5–15
Mass (10^{13} g).....	6.9	2.6	2.5	2.9
Thermal energy content (10^{28} ergs).....	3.4	2.6	4.3	10
Kinetic energy ^a (10^{28} ergs).....	8.6	3.3	3.1	3.6

NOTE.—Here it is assumed that the line-of-sight length of the expanding loop is $8 \times 10^3 \text{ km}$.

^a Kinetic energy was calculated using the derived mass and velocity of 500 km s^{-1} .

TABLE 6
PHYSICAL PARAMETERS OF THE FLARE LOOP

Time (UT)	Temperature (MK)	Density (10^{10} cm^{-3})	Pressure (dyn cm^{-2})	Mass (10^{14} g)	Thermal Energy Content (10^{29} ergs)
09:24:18–09:24:50.....	7.1–18	0.8–6.7	20–200	1.4 ± 0.1	3.7 ± 0.3
09:24:58–09:25:58.....	8.2–20	1.4–12	41–310	1.8 ± 0.1	5.2 ± 0.4
09:26:14–09:30:26.....	9.1–22	2.3–18	69–490	3.7 ± 0.1	11 ± 1
09:30:46–09:34:18 ^a	8.3–21	2.4–19	73–530	3.8 ± 0.1	10 ± 1

^a The physical parameters in the position corresponding to the saturated pixel are not included.

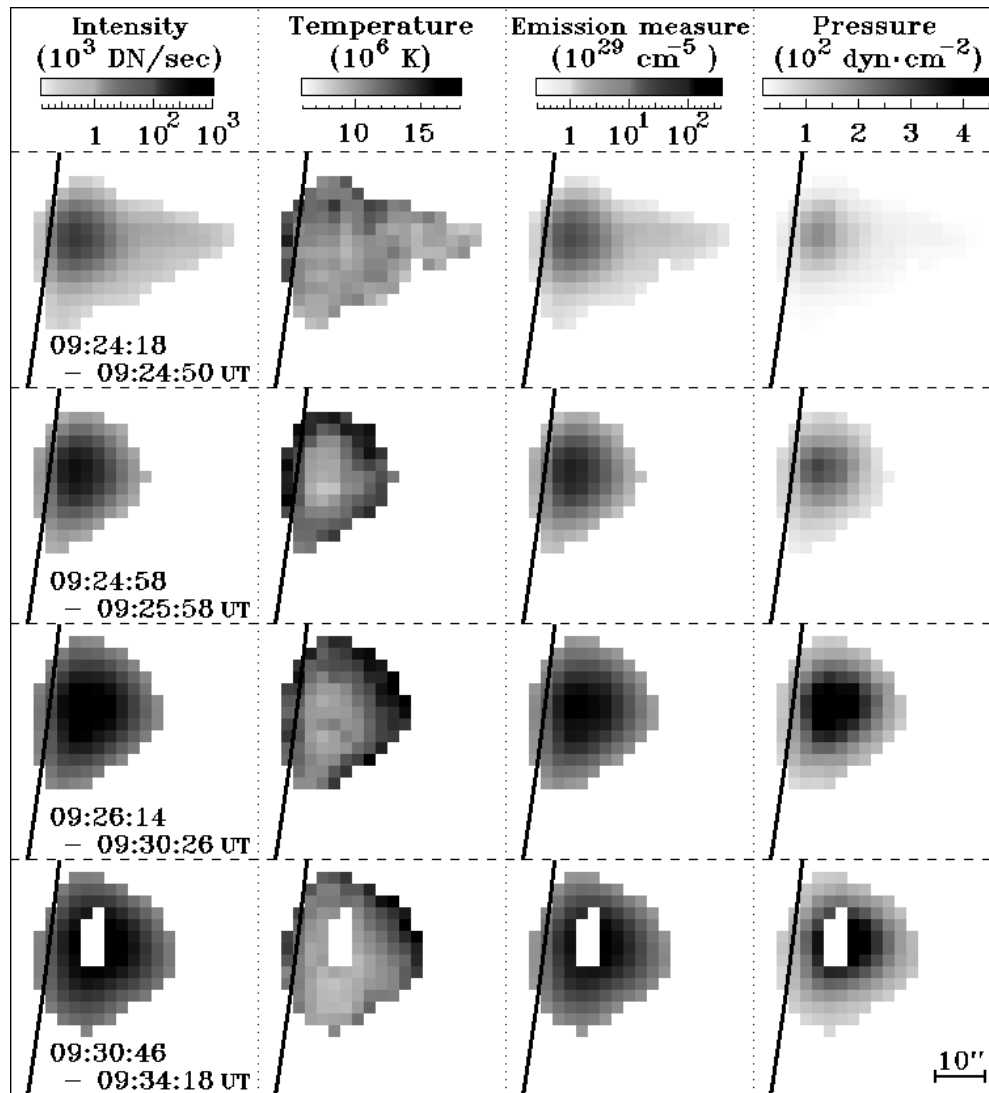


FIG. 9.—X-ray intensity, temperature, emission measure, and pressure maps of the flare on 1992 October 5. These maps were derived after summing temporally and assuming a line-of-sight length of 10^4 km.

loop. The physical parameters of the flare loop are summarized in Table 6. The parameter values increased between 09:24 and 09:34 UT.

4. DISCUSSION

4.1. Morphology and Intensity of the X-Ray Ejecta

The expanding loop appeared to penetrate or be connected with the plasmoid because it expanded with the rise of the plasmoid (Fig. 4). This is consistent with a three-dimensional view of a plasma ejection in the reconnection model (Fig. 10a). Figure 4c, however, shows the loop only on the one side of the plasmoid. The reason is that the expanding loop on the other side may be hidden by a bright structure and/or be too cool to be seen by SXT.

It is interesting that the intensity of the top (plasmoid) of the expanding loop was an order of magnitude stronger than that of its other part. We discuss some possibilities for the cause of this puzzling feature. First, we examine the projection effect. If the density, temperature, and filling factor of the loop (including the plasmoid) are uniform, the ratio of the intensity of the plasmoid to that of the loop

corresponds to the ratio of the line-of-sight length of the plasmoid to that of the loop. We assume that the loop is nearly semicircular and that the external and internal radii are r_1 and r_2 , respectively (Fig. 11a). The line-of-sight lengths of the loop and plasmoid are expressed as l ($=r_1 - r_2$) and l_p [$=2(r_1^2 - r_2^2)^{1/2}$], respectively. Since the intensity of the plasmoid was 20 times stronger than that of the loop (Fig. 5), l_p is 20 times as long as l :

$$(l_p =) 2\sqrt{r_1^2 - r_2^2} = 20(r_1 - r_2) (=20l). \quad (1)$$

From this, we find

$$r_2 = \frac{99}{101}r_1. \quad (2)$$

If r_1 is assumed to be 5×10^4 km (Fig. 4), l is ~ 1000 km. In comparison with the width of the loop in Figure 4c (~ 8000 km), the estimated line-of-sight length of the loop will be too short.

If the pressure in the loop is constant and the temperature at its top is 1.5 times cooler than that at the legs, the density and volume emission measure at the top is 1.5 times and 1.5^2 times larger than those at the legs,

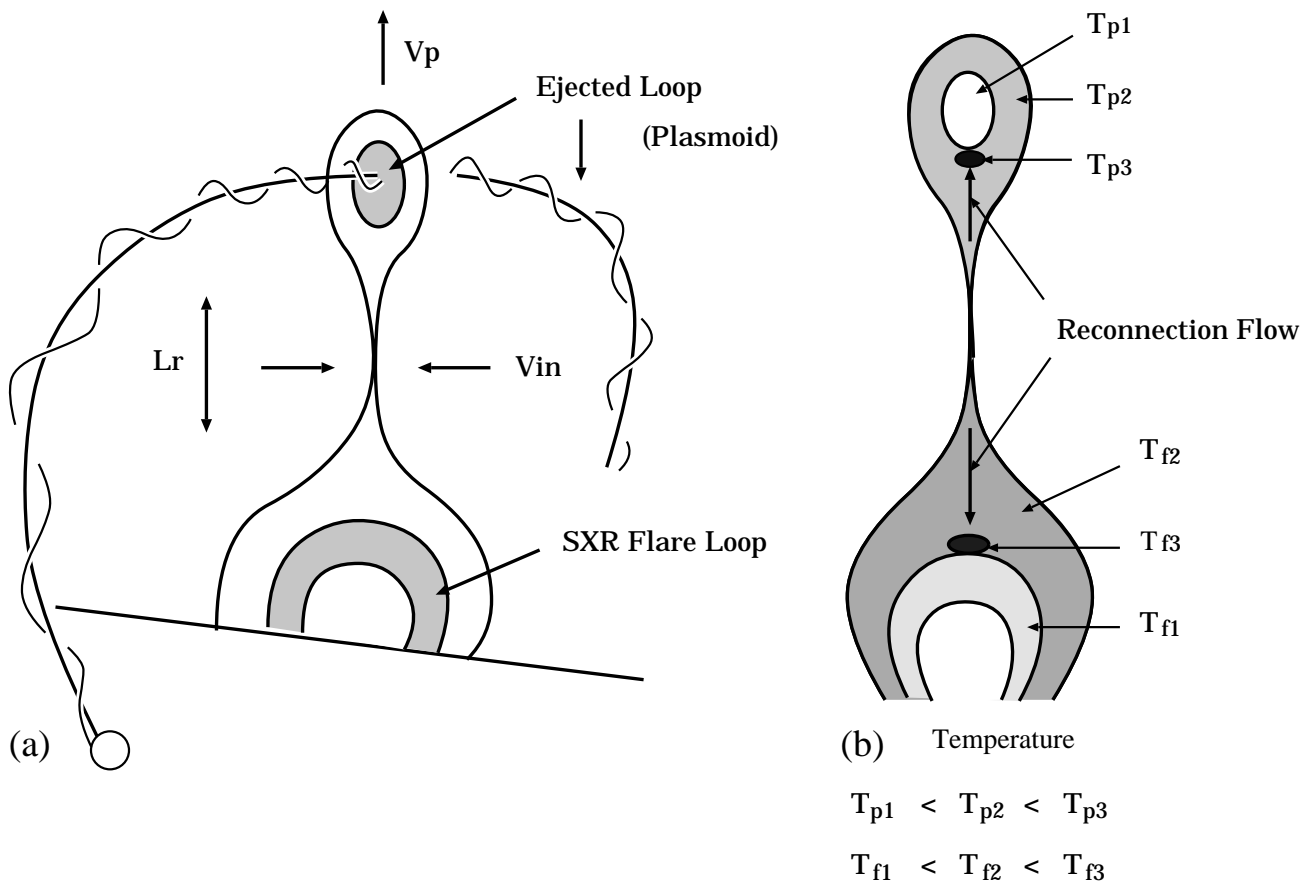


FIG. 10.—(a) Three-dimensional view of the plasma ejection. (b) Temperature distribution of the ejected material and flare loop predicted by the theoretical model (e.g., Yokoyama & Shibata 1997).

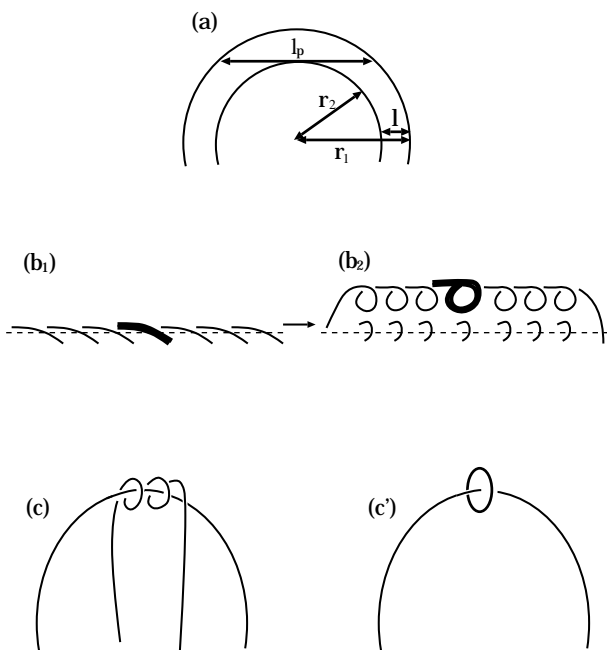


FIG. 11.—Explanations of the puzzle that the intensity of the top of the ejected loop was stronger than that of its other part. (a) The projection effect. (b) If one of the sheared loops before reconnection is denser due to chromospheric evaporation (b_1), in the helical loop its position will be denser after reconnection (b_2). (c) A helical field with high density surrounds the top of the ejected loop. (c') A magnetic field with high density is closed near the top of the ejected loop.

respectively. Then, we find

$$2\sqrt{r_1^2 - r_2^2} = \frac{20}{1.5^2} (r_1 - r_2)$$

$$l = r_1 - r_2 \sim 4800 \text{ [km]} . \quad (3)$$

This is again smaller than the apparent width of the expanding loop. Hence, in the case that the effect of the filling factor is not considered, the projection effect alone cannot easily explain the puzzle that the intensity of the plasmoid was an order of magnitude stronger than that of the loop.

We shall consider other possibilities (Figs. 11b, 11c, 11c'). (1) The lowest lying and strongest sheared loops are seen in the preflare configuration, and a helical loop is formed through reconnection of the sheared loops. If one of the sheared loops is denser for some reason (e.g., the chromospheric evaporation) before main reconnection (Fig. 11b₁), the region corresponding to the dense loop is denser than the other part even after the reconnection (Fig. 11b₂). (2) There is a possibility that a helical magnetic field confines dense plasma at the top of the ejected loop (Fig. 11c). As a special case, we may consider that the field lines making the dense loop are closed near the top of the ejected loop (Fig. 11c').

The intensity of the inner region of the plasmoid was larger than that of its outer region (Fig. 6). This feature is different from the X-ray intensity distribution of an X-ray

plasma ejection associated with an LDE flare on 1992 February 21 (Fig. 12 [Pl. 25]) where the inner region of the ejecta was void (Hudson 1994; see Tsuneta 1996 for other characteristics of the 1992 February 21 flare). Two possibilities for the cause of the weaker intensity for the inner region of the ejecta associated with the 1992 February 21 flare are that (1) the plasma in the inner region of the ejecta had lower density and (2) although there was dense plasma, it could not be detected by SXT because its temperature was too low.

4.2. Physical Conditions of the Plasma Ejection

We now discuss the physical conditions of the ejecta and flare loop. A reconnection model in which magnetic reconnection occurs in the vertical current sheet above a flare loop predicts the following temperature structure (Fig. 10*b*; see also Yokoyama & Shibata 1997): (1) The temperature of the outer region (T_{f2}) is higher than that of the flare loop (T_{f1}). (2) The temperature of the outer region (T_{f2}) is lower than that of the post-fast-shock region (T_{f3}) produced by collision of the reconnection flow with the flare loop. (3) The temperature of the outer region (T_{p2}) is higher than that of the plasmoid (T_{p1}). (4) The temperature of the outer region (T_{p2}) is lower than that of the post-fast-shock region (T_{p3}) just below the plasmoid. The observed temperature structure in this flare is consistent with item (1) (Figs. 6, 7, and 9). However, we cannot clearly confirm (2), (3), or (4) from the present observation, although Figure 6 seems to show some tendency toward supporting the model given by Yokoyama & Shibata (1997).

If an ejected plasma stretches the overlying magnetic fields to form a current sheet leading to reconnection (as assumed in some flare models, e.g., Sturrock 1992), the kinetic energy of the ejected plasma must be larger than the thermal energy content of the flare loop because the magnetic free energy responsible for the flare heating has to be created by the motion of the ejecta. We found that in the 1992 October 5 flare, the kinetic energy of the ejecta was smaller than the thermal energy content of the flare loop, and consequently, the result does not support the hypothesis. The current sheet formation and the plasma ejection are suggested to be the result of a common driving process such as a global MHD instability (e.g., Sakurai 1989; Biskamp & Welter 1989; Mikic & Linker 1994; Kusano, Suzuki, & Nishikawa 1995; Choe & Lee 1996).

4.3. Reconnection Inflow and Reconnection Rate

The reconnection model (Fig. 10) predicts an inflow into the reconnection point. However, no such inflow (or inflow-like structure) has been found in this event. (This is also true for almost all flares observed by SXT aboard *Yohkoh*. This is probably because SXT cannot measure a Doppler shift.) What is the velocity of the inflow expected from observations when we apply the reconnection model (Fig. 10)? According to the reconnection model, the energy release rate is given by

$$\frac{dE}{dt} = 2 \frac{B^2}{4\pi} V_{in} L^2, \quad (4)$$

where B is the magnetic flux density, L is the length of the reconnection region, and V_{in} and $B^2 V_{in}/(4\pi)$ are the velocity of the inflow and the Poynting flux flowing into the recon-

nection region (from one side of the current sheet). If L is assumed to be half of the distance between the ejecta and the flare loop, L is $\sim 10^4$ km at the peak of the hard X-ray emission ($\sim 09:25$ UT). B is estimated by assuming the following pressure balance:

$$P_{in} = P_{out} + \frac{B_{out}^2}{8\pi} [\text{dyn cm}^{-2}], \quad (5)$$

where P_{in} and P_{out} are gas pressures inside and outside the current sheet, respectively. The current sheet is not seen in Figure 6 because, probably, the current sheet is much narrower than one pixel size (~ 1800 km) of the SXT. Hence, P_{in} and P_{out} are assumed to be the pressure of the top and external region of the flare loop, respectively. Since P_{in} and P_{out} are ~ 220 and ~ 20 dyn cm $^{-2}$ from the observed pressure distribution (Fig. 7), respectively, B_{out} is estimated to be ~ 70 G. For simplicity, we assume dE/dt to be dE_{th}/dt , where E_{th} is the thermal energy content of the flare. Here, from Table 6, dE_{th}/dt is

$$\frac{dE_{th}}{dt} \sim \frac{(5.2 - 3.7) \times 10^{29}}{60} = 2.5 \times 10^{27} [\text{ergs s}^{-1}]. \quad (6)$$

Then, we find $V_{in} \sim 30$ km s $^{-1}$. The Alfvén velocity, V_A , is expressed as

$$V_A = \frac{B_{out}}{\sqrt{4\pi\rho}} = \frac{B_{out}}{\sqrt{4\pi N_p m_p}}, \quad (7)$$

where N_p is the proton number density just outside the current sheet, and m_p is the proton mass, 1.67×10^{-24} g. Since the current sheet is not seen in Figure 6, N_p is assumed to be the density of the outer region of the ejecta ($\sim 8 \times 10^9$ cm $^{-3}$). The Alfvén velocity is then ~ 1700 km s $^{-1}$, and the reconnection rate ($M_A = V_{in}/V_A$) is ~ 0.02 . It is interesting to note that this value is consistent with the value expected from the fast reconnection model (e.g., Petschek 1964).

5. CONCLUSION

The 1992 October 5 flare was associated with an X-ray plasma ejection. The ejected material consisted of not only a bloblike feature (plasmoid) but also a loop structure. Although short-exposure images show only the plasmoid, in long-exposure images the plasmoid appeared to be penetrated by or connected to a large-scale expanding loop at its top part. The X-ray intensity of the top (plasmoid) of the expanding loop was about 20 times stronger than that of its other part. It is difficult to explain the puzzle by the projection effect, and we suggest the confinement of the dense plasma by helical fields or closed fields. The intensity of the inner region of the plasmoid was larger than that of its outer region. This is different from the feature of an X-ray plasma ejection associated with the LDE flare on 1992 February 21 (Hudson 1994) where the inner region of the ejecta was void.

The ejected material started to rise before the main peak of the hard X-ray emission, although its initial altitude is not known because it was apparently hidden by the flare loop in the early phase. The ejected material was accelerated during the impulsive phase with velocity from ~ 250 to ~ 500 km s $^{-1}$.

We derived the physical parameters of the ejected material (plasmoid and expanding loop) using the soft X-ray images. The physical parameters of the plasmoid are obtained using the filter ratio method because the plasmoid was observed with multiple filters. Since the expanding loop was taken only with one filter, its physical parameters are derived by assuming that its temperature is equal to the temperature of the plasmoid. The temperature of the plasmoid was 10.6 ± 3.6 MK. The overall temperature structure of the plasma ejection was roughly consistent with that predicted by the reconnection model (e.g., Yokoyama & Shibata 1997), although there was no signature of a fast shock in SXT images of this flare. The density of the plasmoid was $(8-16) \times 10^9 \text{ cm}^{-3}$, which was an order of magnitude larger than that of the typical active-region corona, 10^9 cm^{-3} . Although the density of the expanding loop, $(1-3) \times 10^9 \text{ cm}^{-3}$, was lower than that of the plasmoid, the mass and kinetic energy of the former were factors of 2 or 3 larger than those of the latter. The total mass of the ejected

material was $\sim 2-4 \times 10^{13}$ g. The kinetic energy of the ejecta, $\leq 6 \times 10^{28}$ ergs, was smaller than the thermal energy content of the flare loop, $\sim 5 \times 10^{29}$ ergs. This result does not support the model that an ejected plasma stretches the overlying magnetic fields to form a vertical current sheet leading to reconnection. We suggest that both the ejection and the reconnection are a consequence of a common driving instability.

The *Yohkoh* mission is a project of the ISAS, Japan, with substantial participation from other institutions within Japan and with important contributions from the research groups in the US and the UK under the support of NASA and SERC. The authors would like to thank T. Sakurai, E. Hiei, Ta. Watanabe, H. S. Hudson, and A. Sterling for many useful comments on the manuscript, and S. Tsuneta, K. Akita, T. Yokoyama, and M. Magara for useful discussion. We would like to thank all of the *Yohkoh* team members.

APPENDIX

If the plasmoid is spheroidal, the line-of-sight length of each pixel within the plasmoid is not constant. We shall estimate the line-of-sight length of each pixel assuming that the plasmoid are spheroidal. Figure 13a shows that an ellipse is overlaid on the plasmoid, which is the region within the box in the X-ray image at 09:25:18 UT in Figure 6. The coordinate system is chosen as follows Figure 13a: the x -axis is normal to the plane, and the y - and z -axes are in the direction of north and west, respectively. The spheroid is axisymmetric with respect to the z -axis, and the line-of-sight length is along the x -axis. If the unit

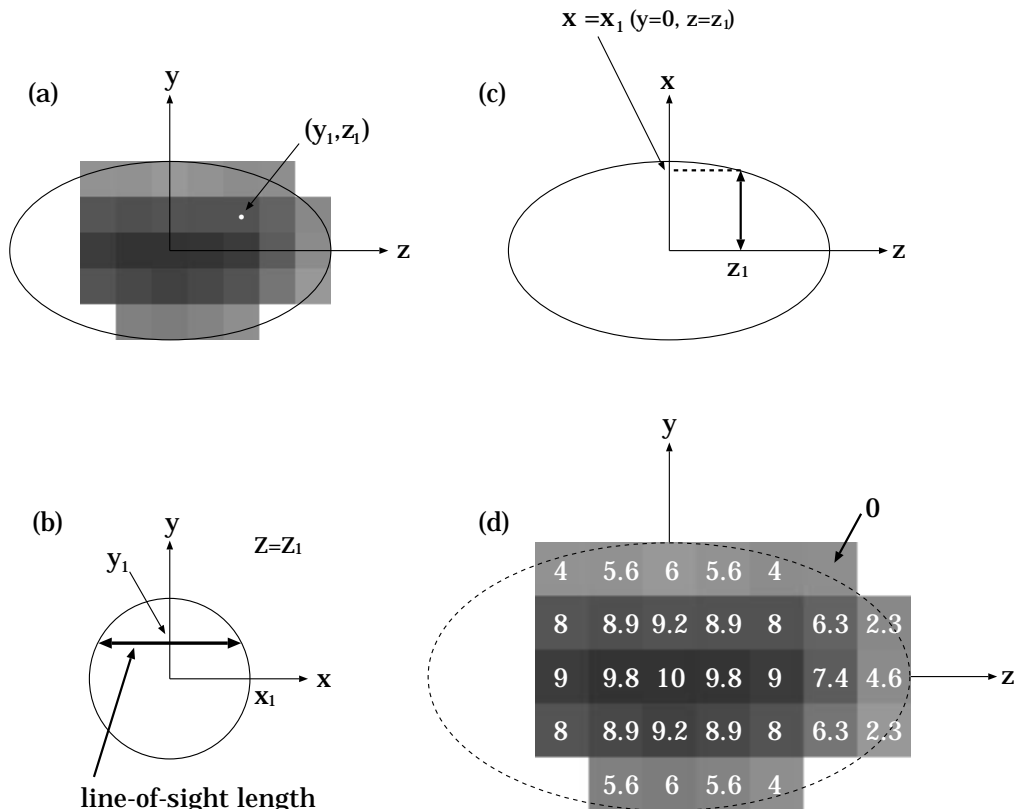


FIG. 13.—(a) An ellipse is overlaid on the plasmoid, which is the region within the box in the X-ray image at 09:25:18 UT in Fig. 6. (b) The x - y plane when $z = z_1$. The line-of-sight length is indicated by the thick line. (c) The section when $y = 0$. The radius of the circle in (b) is x_1 . (d) The value of the line-of-sight length for each pixel, in units of 10^3 km. The value is calculated using the point of the center of each pixel. There is a pixel where the estimated length is imaginary because its center is outside of the ellipse. In the imaginary case, the line-of-sight length of the pixel is assumed to be zero.

of the length in the system is one-half of a pixel size of the X-ray image, the ellipse is given by

$$\left(\frac{y}{5}\right)^2 + \left(\frac{z}{9}\right)^2 = 1. \quad (\text{A1})$$

We shall calculate the line-of-sight length for a point (y_1, z_1) . Figure 13b shows the x - y plane when $z = z_1$. If the radius of the circle is assumed to be x_1 , the line-of-sight length (L) for the point (y_1, z_1) , which is indicated by the thick line, is expressed as

$$L = 2\sqrt{x_1^2 - y_1^2}. \quad (\text{A2})$$

Here, x_1 is the length for $z = z_1$ on the section when $y = 0$ (Fig. 13c). The section is given by

$$\left(\frac{x}{5}\right)^2 + \left(\frac{z}{9}\right)^2 = 1, \quad (\text{A3})$$

and then x_1 is

$$x_1 = 5\sqrt{1 - \left(\frac{z_1}{9}\right)^2}. \quad (\text{A4})$$

The line-of-sight length for the point (y_1, z_1) is given by substituting equation (A4) into equation (A2). We used the point of the center of each pixel as the value of y_1 and z_1 . The value of the line of sight of each pixel is described in Figure 13d, and it is in units of 10^3 km. In the case of using the point of the center of each pixel, there is a pixel where the estimated length is imaginary because its center is outside of the ellipse. Thus, we assumed the line-of-sight length to be zero in the case of imaginary numbers.

REFERENCES

- Akita, K. 1994, Jpn. Astron. Soc. Fall Meeting, S28x
 Biskamp, D., & Welter, H. 1989, Sol. Phys., 120, 49
 Carmichael, H. 1964, in *The Physics of Solar Flares*, ed. W. N. Hess (NASA SP 50) (Washington DC: NASA), 451
 Choe, G. S., & Lee, L. 1996, ApJ, 472, 372
 Forbes, T. G., & Acton, L. W. 1996, ApJ, 459, 330
 Forbes, T. G., & Priest, E. R. 1982, Sol. Phys., 84, 169
 Gerassimenko, M., & Nolte, J. 1978, Sol. Phys., 60, 299
 Hara, H., Tsuneta, S., Lemen, J., Acton, L., & McTiernan, J. 1992, PASJ, 44, L135
 Hirayama, T. 1974, Sol. Phys., 34, 323
 Hudson, H. 1994, in *Proc. Kofu Meeting, A New Look at the Sun with Emphasis on Advanced Observations of Coronal Dynamics and Flares*, ed. S. Enome & T. Hirayama (Nobeyama Radio Observatory Report 360) (Nagano, Japan: Nobeyama Radio Obs.), 1
 Kopp, R. A., & Pneuman, G. W. 1976, Sol. Phys., 50, 85
 Kosugi, T., & Shibata, K. 1997, in *Magnetic Storms*, ed. B. Tsurutani (Washington DC: AGU), 22
 Kosugi, T., et al. 1991, Sol. Phys., 136, 17
 Kusano, K., Suzuki, Y., & Nishikawa, K. 1995, ApJ, 441, 942
 Magara, T., Mineshige, S., Yokoyama, T., & Shibata, K. 1996, ApJ, 466, 1054
 Masuda, S. 1994, Ph.D. thesis, Univ. Tokyo
 Masuda, S., Kosugi, T., Hara, H., Sakao, T., Shibata, K., & Tsuneta, S. 1995, PASJ, 47, 677
 Masuda, S., Kosugi, T., Hara, H., Tsuneta, S., & Ogawara, Y. 1994, Nature, 371, 495
 Mikic, Z., & Linker, J. 1994, ApJ, 430, 898
 Moore, R. L., & Roumeliotis, G. 1992, in *Eruptive Solar Flares*, ed. Z. Švestka, B. V. Jackson, & M. E. Machado (New York: Springer), 69
 Nitta, N. 1996, in *ASP Conf. Proc. 111, Magnetic Reconnection in the Solar Atmosphere*, ed. B. Bentley & J. Mariska (San Francisco: ASP), 156
 Ogawara, Y., Takano, T., Kato, T., Kosugi, T., Tsuneta, S., Watanabe, T., Kondo, I., & Uchida, Y. 1991, Sol. Phys., 136, 1
 Ohya, M., & Shibata, K. 1996, in *Magnetodynamic Phenomena in the Solar Atmosphere*, ed. Y. Uchida, T. Kosugi, & H. S. Hudson (Dordrecht: Kluwer), 525
 ———. 1997, PASJ, 49, 249
 Ohya, M., Shibata, K., Yokoyama, T., & Shimojo, M. 1997, Adv. Space Res., 19, 1849
 Petschek, H. E. 1964, in *The Physics of Solar Flares*, ed. W. N. Hess (NASA SP 50) (Washington DC: NASA), 425
 Sakurai, T. 1989, Sol. Phys., 121, 347
 Shibata, K. 1996, Adv. Space Res., 17, 197
 Shibata, K., Masuda, S., Shimojo, M., Hara, H., Yokoyama, T., Tsuneta, S., Kosugi, T., & Ogawara, Y. 1995, ApJ, 451, L83
 Shibata, K., Nitta, N., Strong, K. T., Matsumoto, R., Yokoyama, T., Hirayama, T., Hudson, H., & Ogawara, Y. 1994, ApJ, 431, L51
 Sturrock, P. A. 1966, Nature, 211, 695
 ———. 1992, in *Eruptive Solar Flares*, ed. Z. Švestka, B. V. Jackson, & M. E. Machado (Berlin: Springer), 397
 Švestka, Z., Farnik, F., Hudson, H., Uchida, Y., Hick, P., & Lemel, J. R. 1995, Sol. Phys., 161, 331
 Tsuneta, S. 1993, in *ASP Conf. Proc. 46, The Magnetic and Velocity Fields of Solar Active Regions*, ed. H. Zirin, G. Ai, & H. Wang (San Francisco: ASP), 239
 ———. 1996, ApJ, 456, 840
 ———. 1997, ApJ, 483, 507
 Tsuneta, S., et al. 1991, Sol. Phys., 136, 37
 Tsuneta, S., Hara, H., Shimizu, T., Acton, L., Strong, K., Hudson, H., & Ogawara, Y. 1992, PASJ, 44, L63
 Tsuneta, S., Masuda, S., Kosugi, T., & Sato, J. 1997, ApJ, 478, 787
 Ugai, M. 1989, Phys. Fluids B, 1, 942
 Vaiana, G. S., Krieger, A. S., & Timothy, A. F. 1973, Sol. Phys., 32, 81
 Yokoyama, T., & Shibata, K. 1997, ApJ, 474, L61